MATERIALS SCIENCE

Dynamic disordering in discrete states: Disconnected hopping boosts anharmonicity in $CuInP_2S_6$

Bowen Wang[1]†, Hejin Yan[1]†, Jie Huang[1,2], Xuefei Yan[3,4], Changmeng Huan[3,4], Johannes Lischner[5], Qingqing Ke[3,4]*, Yongqing Cai[1]*

Delineation of matter into solid and fluid (liquid and gas) phases is grounded in the contrasting localization and mobility of atomic/molecular aggregates, with the fluid phase distinguished by connected pathways for these entities. Here, we demonstrate that $CuInP_2S_6$, a layered material, manifests as a unique system differing from both solid and fluid: It is solid but contains disconnected pathways of highly mobile Cu species. Each pathway comprises two main docking sites, facilitating rapid intersite hopping of Cu that disrupts lattice waves of the immobilized sulfur sublattice, thereby inducing strong phonon anharmonicity. The Cu^+ ions, ordered at low temperatures, become highly activated and dynamically disordered even at room temperature. This suppresses the virial contribution, a dominant heat conduction mechanism in conventional solids, while inducing a moderate liquid-like convective mode of heat transfer. Identifying analogous systems featuring disconnected pathways and dynamical disordering states offers a promising route for increased anharmonicity.

INTRODUCTION

Recent years have witnessed a surge of interest in designing liquid-like solids, an intermediate state of matter between disordered mobile liquid and ordered rigid solid (*1*). Containing at least one type of highly mobile sublattice, these compounds tend to be superionic and exhibit an ultralow thermal conductivity (κ_l) for achieving high-performance thermoelectric, which are critical for next-generation solid systems of energy conversion and storage with high energy density (*2*). Incorporation of local relaxation (i.e., hopping and rotation), with its rate affected by temperature, which competes with the restoring force of vibrations of the immobilized lattice, is critical to induce liquid-like behaviors in solids (*3*). A couple of solid materials with such characteristics, including intercalated two-dimensional (2D) $AgCrSe_2$ (*4*) and Cu_2Se (*5*), among others (*6*), have been found with an ultralow κ_l typically below 1 W m^{-1} K^{-1}. The inherent disordering dynamics in liquid-like solids have inspired the concept of "phonon-liquid electron-crystal" (PLEC) (*5*, *7*), which conducts phonons like a liquid and electrons like a crystal, offering an appealing attribute for designing optimal thermoelectric materials. Beyond the realm of thermoelectrics, liquid-like solids have increasingly garnered attention for their potential in diverse applications, including superionics (*8*), solid electrolytes (*9*), and memristive devices (*10*), and likely achieve long-lived carriers via solvation in chemistry (*11*).

However, the high ionic mobility, a defining characteristic of liquid-like solids, acts as a double-edged sword, elevating the risks of directional segregation, decomposition, and metal deposition of the compounds (*12*). To fully realize the potential of the PLEC concept, it is a prerequisite to address the serious threats to thermodynamic and mechanical stability (*13*). These vulnerabilities are rooted in dual factors at the atomic scale: highly mobile ions and connected diffusion pathways under thermal excitation. Over the past decade, concerted efforts have been devoted to developing strategies for suppressing ion migration at macroscopic scales (*14*). Recent attempts have been directed toward mitigating this challenge through the development of ion-blocking interfaces (*10*) and doping strategies (*2*). Unfortunately, from a thermodynamic standpoint, the flow of highly mobile (*15*) (~10^{-5} cm^2 s^{-1}) and disordered ions in such systems generates large entropy fluctuations, which is accompanied by a substantial fluctuation of the competing enthalpy, seemingly making phase segregation thermodynamically unavoidable.

Here, we demonstrate that the layered $CuInP_2S_6$ (CIPS) material, which differs from conventional solids and liquids with connected diffusive channels, exhibits an immobilized framework and a mobile Cu sublattice with disconnected passages. Equipped with perfectly discontinued channels, we uncover a compelling duality in the dynamics of Cu ions, manifesting as a shift from stable localized vibrations at low temperatures to liquid-like, anisotropic convective dynamics even at ambient conditions. Specifically, these short and constrained pathways are characterized by two docking sites that accommodate Cu atoms, thereby enabling their rapid intersite hopping across a largely shallow bistable potential surface. Furthermore, the lamellar van der Waals (vdW) layers act as physical barriers (*16*), characterized by interlayer migration energies of ~1.1 eV, thereby restricting fluctuations in entropy and enthalpy of Cu^+ ensembles by confining their sampling to the discrete two docking states. The disconnected pathways suppress agglomeration while promoting strong phonon anharmonicity, providing an effective route to achieving ultralow lattice thermal conductivity without sacrificing structural stability.

RESULTS

The atomic structure of CIPS is layered, with each lamella capped by two close-packed sulfur sublayers forming edge-sharing octahedra (Fig. 1A). These planar-aligned octahedra, with three of them per unit cell, each accommodates Cu^+, In^{3+}, and P-P dimers and are arranged in a triangular pattern. Notably, the P-P dimer is vertically aligned, with each phosphorus atom covalently bonded to three sulfur atoms,

[1]Joint Key Laboratory of the Ministry of Education, Institute of Applied Physics and Materials Engineering, University of Macau, Taipa, Macau 999078, China. [2]Department of Applied Physics, Aalto University, Helsinki FI-00076, Finland. [3]School of Microelectronics Science and Technology, Sun Yat-sen University, Zhuhai 519082, China. [4]Guangdong Provincial Key Laboratory of Optoelectronic Information Processing Chips and Systems, Sun Yat-sen University, Zhuhai 519082, China. [5]Department of Materials, Imperial College London, London SW7 2AZ, UK.
*Corresponding author. Email: keqingq@mail.sysu.edu.cn (Q.K.); yongqingcai@um.edu.mo (Y.C.)
†These authors contributed equally to this work.

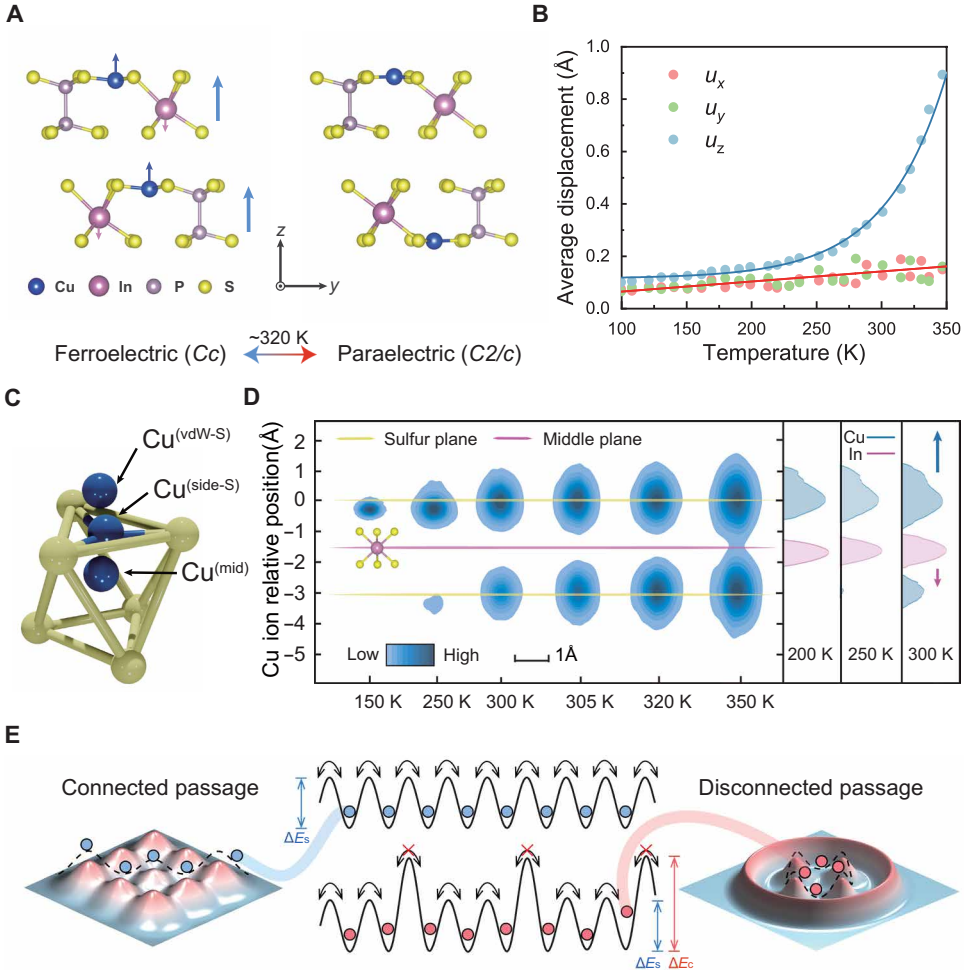

Fig. 1. Dynamic site occupation fluctuations of clamped copper ions in CIPS. (**A**) Phase transition between low-temperature ferroelectric (*Cc*) phases and high-temperature paraelectric (*C2/c*) at ~320 K with ordered and disordered Cu^+ ions, respectively. The blue and pink arrows indicate the relative displacement directions of Cu^+ and In^{3+} ions along the *z* axis, which together give rise to spontaneous polarization and thus the ferroelectric behavior in *Cc* phase. (**B**) Temporally and spatially averaged displacement of Cu^+ along the *x*, *y*, and *z* axes ($u_{x/y/z}$) as a function of temperature. (**C**) Three types of characteristic sites for hosting Cu within an octahedral formed by sulfur atoms: outer-layer $Cu^{vdW\text{-}S}$ sites and stable off-center $Cu^{side\text{-}S}$ and metastable central Cu^{mid} site. (**D**) Contour map of the probability density distribution of Cu^+ within the *xz* section plane at different temperatures. The purple horizontal line marks the middle plane of each layer, while the yellow lines represent the upper and bottom sulfur basal planes. The right is the respective distribution profiles of u_z for Cu and In at different temperatures. (**E**) Illustration of ionic transport pathways under different energy landscapes: Low site-hopping barrier ΔE_s enables connected diffusion channels, while high confinement energy barrier ΔE_c restricts long-range transport, leading to disconnected pathways.

forming an ethane-like $[P_2S_6]^{4-}$ structure. In contrast, the Cu^+ ions form ionic bonds with sulfur atoms, rendering a variability of positions in the octahedral cage, while In^{3+} exhibits a mix of ionic and covalent bonding. Three symmetry distinct Cu configurations are identified on the basis of local coordination environments (Fig. 1C): one stable, off-center framework site coordinated by three nearest sulfur atoms ($Cu^{side\text{-}S}$); two metastable, symmetry-related tetrahedral protrusion sites in the interlayer vdW gap ($Cu^{vdW\text{-}S}$); and a saddle, near-central octahedral site (Cu^{mid}).

The relative occupation of the two $Cu^{side\text{-}S}$ sites on the upper and lower sides depends heavily on the temperature. Above the critical temperature (T_c) of 315 K (*17*), an even dynamic site occupation of Cu^+ ions induces a paraelectric behavior with the reflective *C2/c* space group, whereas below this threshold, an asymmetric distribution of Cu emerges, triggering ferroelectric ordering with the noncentrosymmetric *Cc* space group. This shift is driven by the second-order Jahn-Teller coupling between the filled $3d^{10}$ manifold and the empty 4s orbital (*18*–*20*) of Cu^+, which destabilizes the Cu^+ ions near the sulfur octahedron center. The In^{3+} ion position deviates mildly from the middle plane opposite to Cu^+ (*21*, *22*). Notably, the mechanism underlying ferroelectricity in CIPS layers through frequent intersite hopping of Cu^+ ions differs markedly from conventional ferroelectricity, which arises from displacive sublattice distortion, as exemplified in $BaTiO_3$ (*23*).

The temporally and spatially averaged mean displacement of Cu^+ ions [$\langle u(\mathrm{Cu})\rangle$] from one of the equilibrium $Cu^{(side\text{-}S)}$ position between 100 and 350 K is obtained from molecular dynamics (MD) simulations using moment tensor potentials (MTP) (see Methods for details) (*24*), as shown in Fig. 1B. The displacement components of Cu^+ ions in the in-plane *x* and *y* directions [$\langle u_{x,y}(\mathrm{Cu})\rangle$] are isotropic

and approximately proportional to the temperature with a proportionality constant of 3.85×10^{-4} Å/K, reaching ~0.15 Å at 350 K. In contrast, the out-of-plane component [$\langle u_z(\mathrm{Cu})\rangle$] exhibits an exponential increase with temperature [$< u_z(\mathrm{Cu}) > = u_0 + Ae^{\gamma T}$, fitted γ, u_0, and A parameters provided in table S1], reaching 0.2, 0.37, and 0.89 Å at 250, 300, and 350 K, respectively. The In^{3+} ions follow a similar exponential trend as Cu^+ ions, albeit with significantly smaller displacements (figs. S1 and S2). In contrast, the P and S species exhibit a linear increase in displacement (table S1). This difference lies in the mobile Cu^+ cations and relatively immobilized S^{2-} anions, inducing collective sublattice (de)coupling and ferroic (dis)ordering amenable to temperature. These findings align with experimental observations (*25*), supporting the hypothesis that temperature strongly modulates the amplitude of Cu^+ ion vibrations.

The MD trajectories of Cu^+ ions are traced, and a spatially resolved mapping is shown in Fig. 1D. The contour plots of u_z (Cu) highlight the mobility of Cu even at moderate temperatures, and the distributions of u_z(Cu) and u_z(In) are generated. At 150 K, Cu^+ ions nearly all located on the same side, i.e., the "up" side (classified as Cu^u), mostly at the $Cu^{side\text{-}S}$ about 1.57 Å above the midplane, in excellent agreement with the experimental value of 1.55 Å (*25*). The temperature-dependent occupation probabilities of these sites are further analyzed in detail in fig. S3. As temperature increases, the Cu^+ ions tend to deviate from the up side and hop to the "down" side (labeled as Cu^d), predominantly occupying the $Cu^{side\text{-}S}$ type. The occupations of these previously unidentified Cu^d species are 0, 2, 18, 35, 49, and 50% at 150, 250, 300, 305, 320, and 350 K, respectively. Equal probability of occupation as Cu^u and Cu^d occurs at ~320 K, signifying strong site hopping between upper and lower $Cu^{side\text{-}S}$ sites even at ambient temperature. The evolution of the Cu^+ ion distribution closely matches experimental results (*25*), confirming that the MTP accurately captures the dynamics of CIPS at the atomic scale. Here, the unique bipolar distribution of Cu in CIPS around the two docking sites suggests a disconnected hopping pathway in CIPS, which markedly differ from the connected passage of ions in conventional superionic conductors or the PLEC compounds, as schematically compared in Fig. 1E. In conventional superionic conductors, a string of shallow site-hopping barriers (ΔE_s) merges into a continuous diffusion corridor, allowing the mobile ions to percolate throughout the lattice. In contrast, the conducting pathways of Cu in CIPS are disconnected. While each Cu^+ ion hops frequently between the two vertically aligned docking sites with a low ΔE_s, long-range motion is restricted due to the substantial confinement energy barrier (ΔE_c) preventing migration to neighboring equivalent sites across or within the plane. This energy hierarchy creates rapid yet confined pathways without compromising lattice discontinuity: Cu^+ ions hop briskly within their respective pocket—while the high ΔE_c blocks long-range ionic flow and the instability it would otherwise cause.

Figure 2A shows the phonon dispersion relations (PDR) for the ferroelectric phase of CIPS at 0 and 250 K, calculated using force constants generated from the MTP. The accuracy of the MTP is further validated by its agreement with phonon dispersion curves (fig. S4), energies and forces (fig. S5), and thermal properties (fig. S6) obtained from density functional theory (DFT). In addition, MD simulations performed at several representative temperatures confirm stable lattice dynamics without energy drift or framework atom diffusion (fig. S7). A convergence test for the supercell size used for the PDR calculations is also included (fig. S8). At 250 K, a noticeable redshift in phonon frequencies is observed compared to 0 K, implying significant phononic renormalization. There exists substantial overlap between the low-frequency optical and acoustic branches (<100 cm^{-1}), indicating a strong coupling between these modes. The phonon density of states (PDOS) analysis reveals that the Cu^+ ions mainly contribute to these low-frequency phonon branches, while the P and S ions primarily account for high-frequency optical branches.

The κ_l is obtained by solving the Boltzmann transport equation (BTE), with convergence tests (figs. S9 and S10) and computational details provided in Methods. The κ_l exhibits significant anisotropy and a positive correlation with the inverse temperature (Fig. 2B), consistent with experimental findings (*26*–*28*). Notably, when considering only three-phonon (3ph) scattering processes, the calculated κ_l values at 100 K are 6.03 and 1.86 W m^{-1} K^{-1} along the parallel and perpendicular directions, respectively, overestimating the experimental values of 4.03 and 0.69 W m^{-1} K^{-1}. With the inclusion of four-phonon (4ph) scattering processes, the in-plane and out-of-plane κ_l values decrease markedly to 3.88 and 0.91 W m^{-1} K^{-1}, respectively, closely matching the experimental data. This highlights the critical role of 4ph processes which remain unexpectedly active even down to a relatively low temperature of 100 K, unlike in most 2D materials (*29*, *30*). This can be attributed to a relatively soft lattice of CIPS as indicated by its low Debye temperature (Θ_D) of 130 K. The Θ_D was calculated using the elastic constants method via: $\Theta_D = \frac{h}{k_B}\left(\frac{3n}{4\pi V}\right)^{1/3}\mathbf{v}_m$, where h is the Planck's constant, k_B is the Boltzmann constant, n is the number of atoms per unit cell, V is the unit cell volume, and $\mathbf{v}_m$ is the average sound velocity.

Moreover, the frequency-dependent cumulative κ_l at various temperatures (50, 250, and 350 K) reveals that phonons below 100 cm^{-1} contribute the most to κ_l, as shown in Fig. 2C and fig. S11. These low-frequency branches, predominantly acoustic and rigid-layer quasi-acoustic modes (fig. S12), account for up to ~90% of κ_l (fig. S13), which is in sharp contrast to other 2D materials (*31*). Given the significant contribution of Cu^+ ions in these weak modes (Fig. 2A), it is conceivable that the degree of the Cu sublattice ordering, controlled by thermal disturbances, modulates their coupling with the P-S backbone lattice, explaining the importance of 4ph scattering in limiting the value of κ_l. CIPS exhibits a strong phononic anharmonicity which is also quantified by the Grüneisen parameter $\gamma = -\frac{V_0}{\omega}\frac{\partial \omega}{\partial V}$, where ω is the phonon frequency and V is the equilibrium volume. As shown in fig. S14, the γ is negative for the low-frequency phonon modes (<100 cm^{-1}), reaching a minimum around 50 cm^{-1}, where the Cu vibrations dominate (Fig. 2A). This is caused by a shallow potential energy landscape (*32*) that gives rise to Cu^+ ion displacements that deviate from the typical parabolic distance-energy relationship. Therefore, the large phononic anharmonicity coincides with the ease of Cu^+ ion displacement under thermal excitation.

The strong phononic anharmonicity is further analyzed with respect to the rates of 3ph and 4ph scattering channels within scattering phase space. Relevant channels include 3ph absorption ($\lambda_1 + \lambda_2 \rightarrow \lambda$) and emission ($\lambda \rightarrow \lambda_1 + \lambda_2$) pathways, as well as 4ph splitting ($\lambda \rightarrow \lambda_1 + \lambda_2 + \lambda_3$), redistribution ($\lambda_1 + \lambda_2 \rightarrow \lambda_3 + \lambda_4$), and combination ($\lambda_1 + \lambda_2 + \lambda_3 \rightarrow \lambda$) pathways (Fig. 2D). At 50 K, the 3ph emission process dominates the scattering involving the low-frequency modes (<100 cm^{-1}), as indicated by its substantial volume of the weighted scattering phase space (Fig. 2E). As the temperature increases, the 4ph scattering process becomes increasingly activated, and by 250 K, its volume even surpasses that of 3ph scattering across the entire frequency range. It is noteworthy that the 4ph process

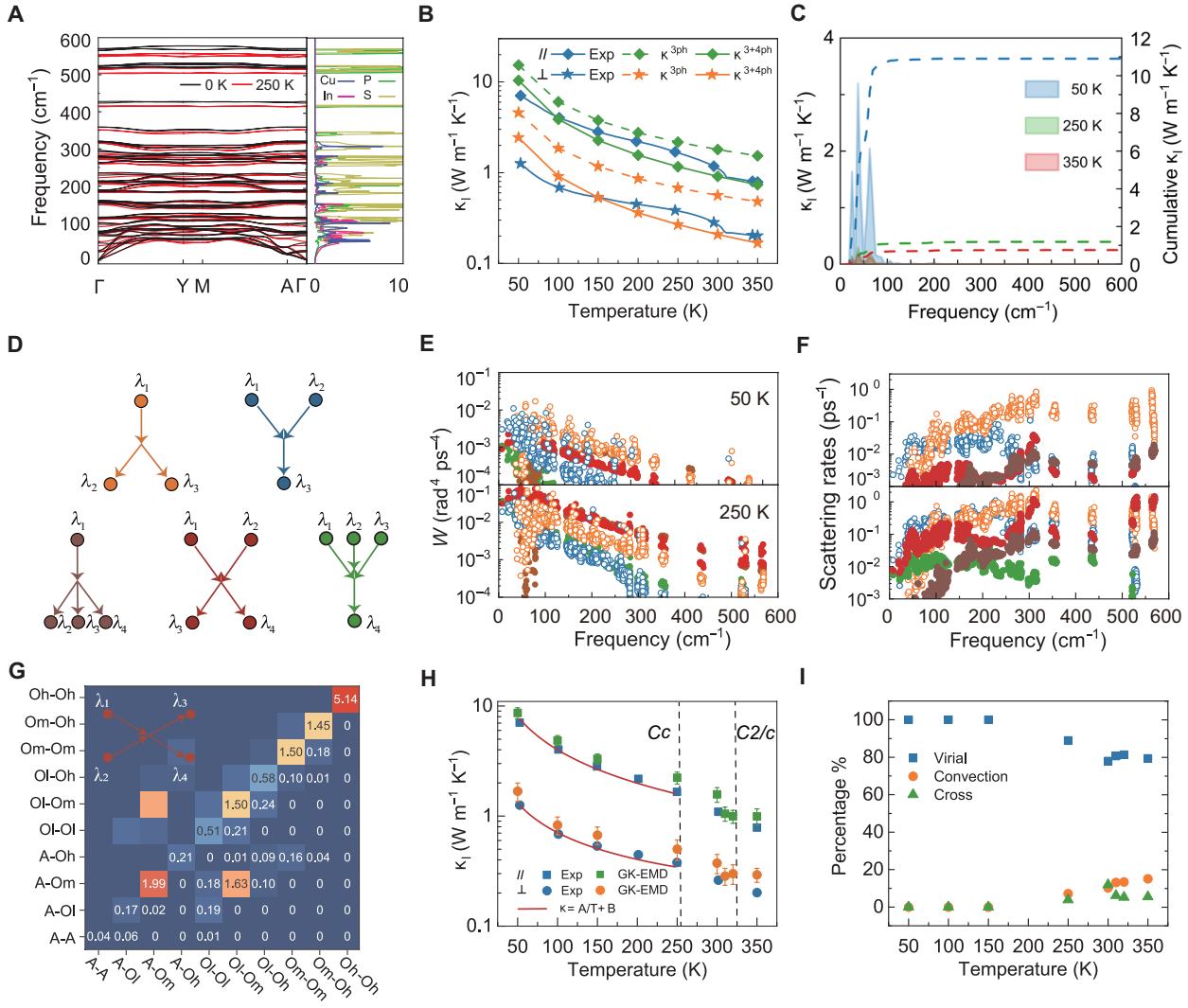

Fig. 2. Phonon scattering and anharmonicity arising from the bistable states of Cu species in CIPS. (**A**) Phonon dispersion obtained by MTP at 0 and 250 K along with partial PDOS calculated from DFT. (**B**) Predicted κ_l along direction parallel (//) and normal (⊥) to basal plane as a function of temperature, considering 3ph and 4ph processes by the BTE approach, compared with experimental data from Kohutych *et al.* (*26*). (**C**) Frequency-resolved (shadowed area) and cumulative (dashed lines) trend of κ_l along parallel direction. (**D**) Schematic diagrams of typical 3ph and 4ph scattering channels. (**E**) Volume (*W*) of phase space for different 3ph and 4ph scattering channels as a function of frequency at 50 and 250 K. (**F**) Scattering rates of 3ph and 4ph channels. (**G**) Heatmap of 4ph redistribution across acoustic (A) and optical (Ol, Om, and Oh) phonons at 250 K, grouped by frequency ranges: Ol (0 to 100 cm^{-1}), Om (100 to 400 cm^{-1}), and Oh (>400 cm^{-1}). (**H**) κ_l as a function of temperature derived using the GK-EMD method, compared with the experimental measurements. (**I**) Contribution of the virial, convective, and cross terms to κ_l at different temperatures.

contributes significantly even at low temperatures where incipient Cu hopping occurs. As shown in Fig. 2F, at 250 K, the scattering rate of the 4ph redistribution process becomes comparable to those of the 3ph processes, within the frequency range of <100 cm^{-1} where thermal conduction predominantly occurs (Fig. 2C). This explains the significant role of the 4ph scattering in limiting the κ_l in Fig. 2B.

The strong phonon-phonon scattering could be rooted in the presence of flat bands in the PDR, which are associated with localized vibrations of Cu, In, and P-P units encaged within the sulfur octahedra. The phonon-phonon scattering pathways at each phonon mode ($\mathbf{q}$, ν) at momentum $\mathbf{q}$ (table S2) of the νth branch are further quantified by counting all 3ph and 4ph interactions that satisfy both energy and momentum conservation. The scattering rate $\Gamma^{(n)}_{\mathbf{q}\nu}$ of a given mode involved in a n-phonon process is computed using the Fermi's golden rule $\Gamma^{(n)}_{\mathbf{q}\nu} = \frac{2\pi}{\hbar} \sum_{\mathbf{q}_1\nu_1,\ldots,\mathbf{q}_{n-1}\nu_{n-1}} |V^{(n)}_{\mathbf{q}\nu,\mathbf{q}_1\nu_1,\ldots,\mathbf{q}_{n-1}\nu_{n-1}}|^2 \delta\left(\omega_{\mathbf{q}\nu} \pm \omega_{\mathbf{q}_1\nu_1} \pm \cdots \pm \omega_{\mathbf{q}_{n-1}\nu_{n-1}}\right) \delta_{\mathbf{q}\pm\mathbf{q}_1\pm\cdots\pm\mathbf{q}_{n-1},\mathbf{G}}$, where $\omega_{\mathbf{q}\nu}$ is the phonon frequency, and $V^{(n)}$ denotes the n-phonon interaction matrix element. The delta function $\delta(\cdots)$ enforces energy conservation, while $\delta \ldots_{,\mathbf{G}}$ ensures momentum conservation. The 3ph emission channels in CIPS (fig. S15) mainly occur via O (optical phonon) → O + O processes. More specifically, this involves Om (middle optical band from 100 to 400 cm^{-1}) → Ol (low frequency optical mode < 100 cm^{-1}) + Om channels. The absorption processes exhibit a similar scattering pathway distribution but with noticeably lower scattering rates compared to emission. For the 4ph channels, redistribution

overwhelmingly dominates, which is roughly two orders of magnitude larger than that of splitting or combination events (fig. S15). From the redistribution heatmap (Fig. 2G), the most intense elements sit in the high-frequency optical band (Oh, >400 cm^{-1}) Oh + Oh → Oh + Oh channels, showing extremely strong 4ph interactions among the high-frequency optical modes, dominantly contributed by sulfur (Fig. 2A). This strength originates from the dense, nearly flat high-frequency branches in the PDR, allowing a large phase space with simultaneously satisfied energy and momentum conservation for the 4ph events. As temperature rises, enhanced population of these modes boosts the rate of the complex redistribution pathway by more than an order of magnitude (Fig. 2F). Substantial weights are also evident in processes involving the acoustic (A) mode: A + Om → A + Om, indicating frequent momentum exchange between the heat-carrying A and Om modes. Such cross-branch redistribution shortens the lifetime of the A modes and broadens their linewidths, hence suppressing the κ_l at the elevated temperatures.

Different from heat conduction in well-localized crystalline solid, reversible site hopping of Cu ions in an approximately bistable potential landscape in CIPS gives rise to dynamic site occupancy fluctuations that affect the thermal conduction. To account for the kinetic intralayer interconversion of Cu, the κ_l is reevaluated using the Green-Kubo equilibrium molecular dynamics (GK-EMD) approach, as presented in Fig. 2H. The associated size effect and convergence tests are shown in figs. S16 and S17, respectively. The heat flux **J** is analyzed and decomposed into two main contributions: a virial term resulting from interatomic interactions $\mathbf{J}_v$ and a convective term associated with moving atoms $\mathbf{J}_c$, such as phonons and diffusive motion (*33*)

$$\mathbf{J}(t)=\mathbf{J}_v(t)+\mathbf{J}_c(t)=\sum_i\sum_{j\neq i}\mathbf{r}_{ij}\left(\frac{\partial e_i}{\partial \mathbf{r}_j}\cdot\mathbf{s}_j\right)+\sum_i e_i\mathbf{s}_i \quad (1)$$

where $\mathbf{r}_{ij}$ is the relative position vector, e_i is the total energy associated with atom i, and $\mathbf{s}_i$ is its velocity. Therefore, we can divide κ_l into contributions from the virial interatomic vibrations (κ_v), the convection of hopping (κ_c), and the cross term related to lattice-convection interactions (κ_{vc}), through integration of autocorrelation of heat flux over time as below

$$\kappa_l=\frac{1}{3k_BT^2}\int_0^\infty\Big[\underbrace{\langle\mathbf{J}_v(t)\cdot\mathbf{J}_v(0)\rangle}_{\text{virial}}+\underbrace{\langle\mathbf{J}_c(t)\cdot\mathbf{J}_c(0)\rangle}_{\text{convection}}+2\underbrace{\langle\mathbf{J}_v(t)\cdot\mathbf{J}_c(0)\rangle}_{\text{cross}}\Big]dt \quad (2)$$

The temperature-dependent κ_l can be broadly categorized into three distinct regimes based on the propensity for Cu^+ hopping (Fig. 2I):

(i) In the low-temperature ferroelectric regime (below 250 K), Cu^+ ions undergo mild deviations from their equilibrium position. Hence, the phonon-related virial term dominates the κ_l, while the κ_c and κ_{vc} components are negligible (Fig. 2I). The κ_l scales with the inverse temperature $\kappa_l \propto 1/T$, in agreement with experiments (*28*) and indicative of the dominant Umklapp scattering mechanism (fig. S18).

(ii) In the proximity of the ferroelectric-paraelectric transition (250 to 320 K), the κ_v remains dominant but decreases by nearly 20% (Fig. 2I). This suppression of the vibrational contribution is consistent with the experimentally observed softening of the longitudinal sound velocity along the *c* axis when approaching $T_c \approx 312$ K, together with a pronounced peak in ultrasonic attenuation (*34*), indicating elastic softening and enhanced vibrational dissipation in the transition regime. The cross and convection terms gain significance with the incipient hopping Cu^+ ions. This leads to a deviation from the $1/T$ law (Fig. 2H) and explains the inflection point in the T-κ_l curve around the critical temperature of 310 K, failed to be reproduced by the above displacive method. At 300 K, immediately before the ferroelectric-paraelectric phase transition, the ratio of κ_v:κ_c:κ_{vc} is 78:12:10. The onset of the convection-related contribution to heat transfer near room temperature, which is absent in common unmelted solids, indicates unique liquid-like characteristics in CIPS.

(iii) In the paraelectric regime ($T \geq$ ~320 K), the κ_l remains nearly stable at low values with the κ_c increases while the κ_v drops steadily with temperature.

To further elucidate the underlying dynamics and structural correlations that vary with temperature, Raman scattering spectra of CIPS were measured (Fig. 3A). With increasing temperature, the peaks around 100, 320, and 550 cm^{-1} exhibit significant broadening and

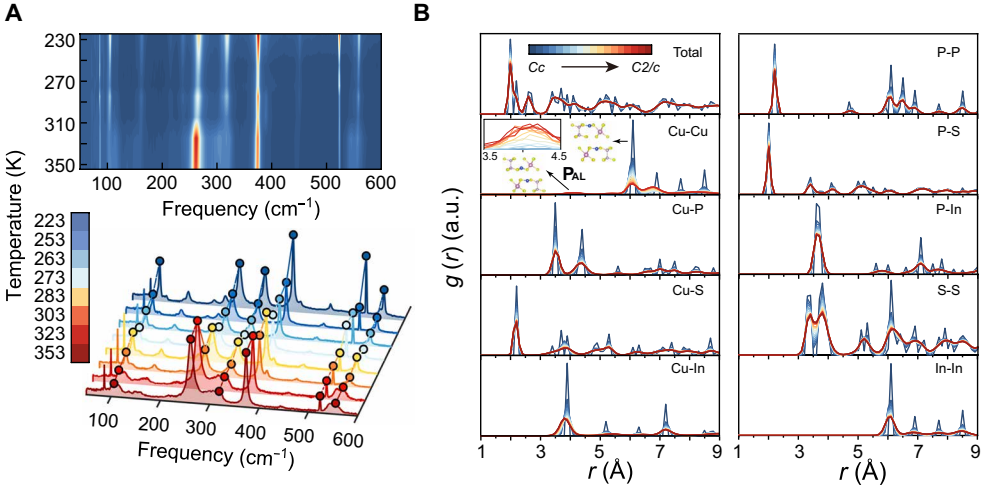

Fig. 3. Signatures of temporal spectrum and spatial correlation due to activated displacive Cu species. (**A**) Experimental Raman scattering spectra of CIPS measured at various temperatures. (**B**) Total and partial PDF of CIPS transiting from the low-temperature *Cc* phase to the high-temperature *C2/c* phase. a.u., arbitrary units.

reduced intensities, indicating the disruption of the long-wavelength oscillations. The 100-cm^{-1} peak with its principal Cu vibrations eventually diminishes as the temperature rises, reflecting that Cu^+ ions convert from an ordering and localized state to a disordering and dynamic behavior. The flattening of the peaks near 320 and 550 cm^{-1}, with their vibrating eigenvector including substantial sulfur component, infers that the Cu hopping broadens the phonon linewidth, consistent with the strong 4ph scattering of these high-frequency modes (Fig. 2, F and G).

The average total and partial pair distribution functions (PDF), $g(r)$, uncover local (dis)ordering triggered by Cu^+ ion hopping within sulfur octahedral during the *Cc* ↔ *C2/c* phase transition (Fig. 3B). The total $g(r)$ has distinct sharp peaks, characteristic of the ferrielectric *Cc* phase at low temperatures. These peaks gradually broaden and weaken as the temperature increases while approaching the paraelectric *C2/c* phase. The leftmost peak, located at ~2 Å, corresponds to the superposition of nearest neighboring P-P and P-S bonds, both of which are relatively insensitive to temperature changes, consistent with their covalent nature.

In contrast, all of those peaks in the PDF involving Cu coordination, specifically Cu-Cu, Cu-P, Cu-S, and Cu-In pairs, undergo strong softening and broadening with temperature, indicative of substantial bond reorganization and sublattice disordering induced by Cu hopping. Notably, the motion of Cu^+ ions triggers an opposite motion of the In^{3+} ions. Those peaks in the partial $g(r)$ of the Cu-Cu and In-In pairs show a greater reduction compared to P-P, S-S, and P-S pairs, suggesting that the disordering is predominantly confined to the Cu and In cationic sublattice, while the backbone P-S lattice remains relatively rigid against thermal disturbances. Upon raising the temperature, a distinct peak (marked as P_{AL}) emerges at ~4 Å in the partial PDF of the Cu-Cu pair, located beside the existing leftmost peak at ~6 Å. This results from the depopulation of Cu^+ ions initially occupying at the same side in each layer at low temperatures, and this shows the onset of phase transition, appearing with the coexistence of the Cu^u and the Cu^d. The P_{AL} peak, which is wide but shallow, manifests the coupling of Cu^u and Cu^d group from adjacent layers. It signifies the split of site occupation and a loss of site polarity, from monotype (Cu^u or Cu^d) to equivalent distributing Cu^u and Cu^d at elevated temperatures. Therefore, it is conceivable that the width and the height of this peak encode the degree of disorder and interlayer coupling.

MD simulations on CIPS structure involving 40 layers up to 40 ns reveal the evolution of site polarity with temperature, defined as the Cu^d:Cu^u population ratio as shown in Fig. 4A. The hopping probabilities and time (τ) of Cu^+ ions are obtained by a series of independent simulations with different temperatures (Fig. 4B). At 250 K, Cu^+ ions predominantly maintain as the initially set Cu^u type at the $Cu^{side\text{-}S}$ site, and their migration is relatively infrequent with a low flip probability (~0.78%). As temperature rises above 250 K, redistribution from Cu^u to Cu^d occurs gradually while the τ remains approximately constant, indicating a stable intersite hopping dynamics. At ~300 K, a sharp transition occurs, marked by an inflection in the content of Cu^u type and a sudden drop of the τ. The system reaches equilibrium at ~325 K, where the content of Cu^u type species levels off. The flip probability of Cu^+ ions increases further with temperature, reaching nearly 20% at 350 K. Concurrently, the average τ decreases significantly from ~20 ps at 300 K to ~13 ps at 350 K, indicating that not only are more Cu^+ involved in the hopping process, but each hopping event also occurs on a shorter timescale at elevated temperatures, facilitating a faster ionic transport within the material. It is evident that at a moderate temperature of 300 K, a significant number of Cu^+ ions are already uniformly inverted throughout CIPS. Notably, the spatial distributions of Cu^+ ions at 320 and 350 K differ entirely due to temperature-dependent hopping dynamics, which reshape the local configurations and produce distinct percolating domain-like patterns (Fig. 4A), despite a free of site polarity.

The single-particle dynamics of Cu^+ ions are quantified through constructing incoherent intermediate scattering function defined as $F_{\text{incoh}}(\mathbf{q}, t) = = \frac{1}{N}\sum_i^N \langle \exp[i\mathbf{q}\cdot(\mathbf{r}_i(t) - \mathbf{r}_i(0))]\rangle$, where N is the number of Cu atoms, and $\mathbf{r}_i(t)$ is the position of atom i at time t. Here, $\mathbf{q}$ is the reciprocal-space vector with units of inverse length (in unit of per angstrom), derived by converting fractional coordinates along high-symmetry paths in the Brillouin zone into Cartesian vectors using the reciprocal lattice basis from the simulation cell. Along the in-plane direction $\mathbf{q} = (k, k, 0)$ (Fig. 4C), the F_{incoh} profiles at 250 and 350 K retain nearly undamped sinusoidal oscillations, an indicative of a solid-like and high localization of Cu species along in-plane directions. In contrast, along the out-of-plane direction $\mathbf{q} = (0, 0, k)$, there exhibits a temperature-dependent crossover reflecting a transit from vibrational to diffusive-like kinetics: at 250 K (Fig. 4D) the F_{incoh} showing a heavily damped oscillator that settles to a small negative baseline, indicative of intermittent jump diffusion of Cu species superimposed on their local vibrations, while at 350 K (Fig. 4E) a straight negative decay with a barely quenched oscillation, a typical behavior of atomic diffusion. In contrast, the F_{incoh} of all other elements (P, S, and In) maintain the regular oscillation over time and hence solid-like vibrating behaviors both at 250 and 350 K (figs. S19 to S22).

Building on the F_{incoh} which essentially depicts the correlation of atomic density, relying on atomic positions, next, we perform similar analysis with introducing atomic current $\mathbf{j}$, governed instead by atomic velocity $\mathbf{s}_i$ via $\mathbf{j}(\mathbf{q}, t) = \sum_i^N \mathbf{s}_i(t)e^{i\mathbf{q}\cdot\mathbf{r}_i(t)}$. The $\mathbf{j}(\mathbf{q},t)$ can be further decomposed into the transverse $\mathbf{j}_T(\mathbf{q},t)$ and longitudinal $\mathbf{j}_L(\mathbf{q},t)$ components relative to $\mathbf{q}$ direction. Further, the correlation of the current entails the transversal component $C_T(\mathbf{q}, t) = \frac{1}{N}\langle \mathbf{j}_T(\mathbf{q}, t)\cdot\mathbf{j}_T(-\mathbf{q}, 0)\rangle$, and the longitudinal one $C_L(\mathbf{q}, t) = \frac{1}{N}\langle \mathbf{j}_L(\mathbf{q}, t)\cdot\mathbf{j}_L(-\mathbf{q}, 0)\rangle$, both of which are the primary contributors of heat conduction. The Fourier transform of $C_{T\text{-}L}(\mathbf{q},t)$ in temporal space, defined as the difference between $C_T(\mathbf{q},t)$ and $C_L(\mathbf{q},t)$, generates dynamic correlation $C_{T\text{-}L}(\mathbf{q},\omega)$ defined in frequency space. Partial $C_{T\text{-}L}(\mathbf{q},\omega)$ for selected atomic pairs (i.e., Cu-S) allows to reveal the degree of their coupling and lattice dynamics (figs. S23 to S29).

Figure 4F shows the high-symmetry path Γ-Y-M-A-Γ in the Brillouin zone, along which the Cu-projected $C_{T\text{-}L}(\mathbf{q},\omega)$ is compared at 250 and 350 K in Fig. 4 (G and H). At 250 K, the transverse current channel manifests itself as a remarkably flat, intense band centered at ~60 cm^{-1} along Γ → Y (in-plane rigid-layer shearing modes) and a dispersion along Γ → A (out-of-plane flexural branch), whereas the longitudinal current coincides with the bulk longitudinal and rigid-layer compressive branch along Γ → A. This again infers a strong anisotropy in the $\mathbf{s}_{Cu}$ field: In-plane collective motion is predominantly shear like, while out-of-plane motion is compressional. Upon heating to 350 K, significant broadening of the current branches occurs which underscores phononic anharmonicity driven by the dynamic disordering caused by frequent Cu intersite hopping with equal Cu^u and Cu^d population. Each stochastic jump disrupts phase coherence of the atomic current, shortening the correlation time. In contrast, the P-P and S-S pairs are less sensitive to temperature

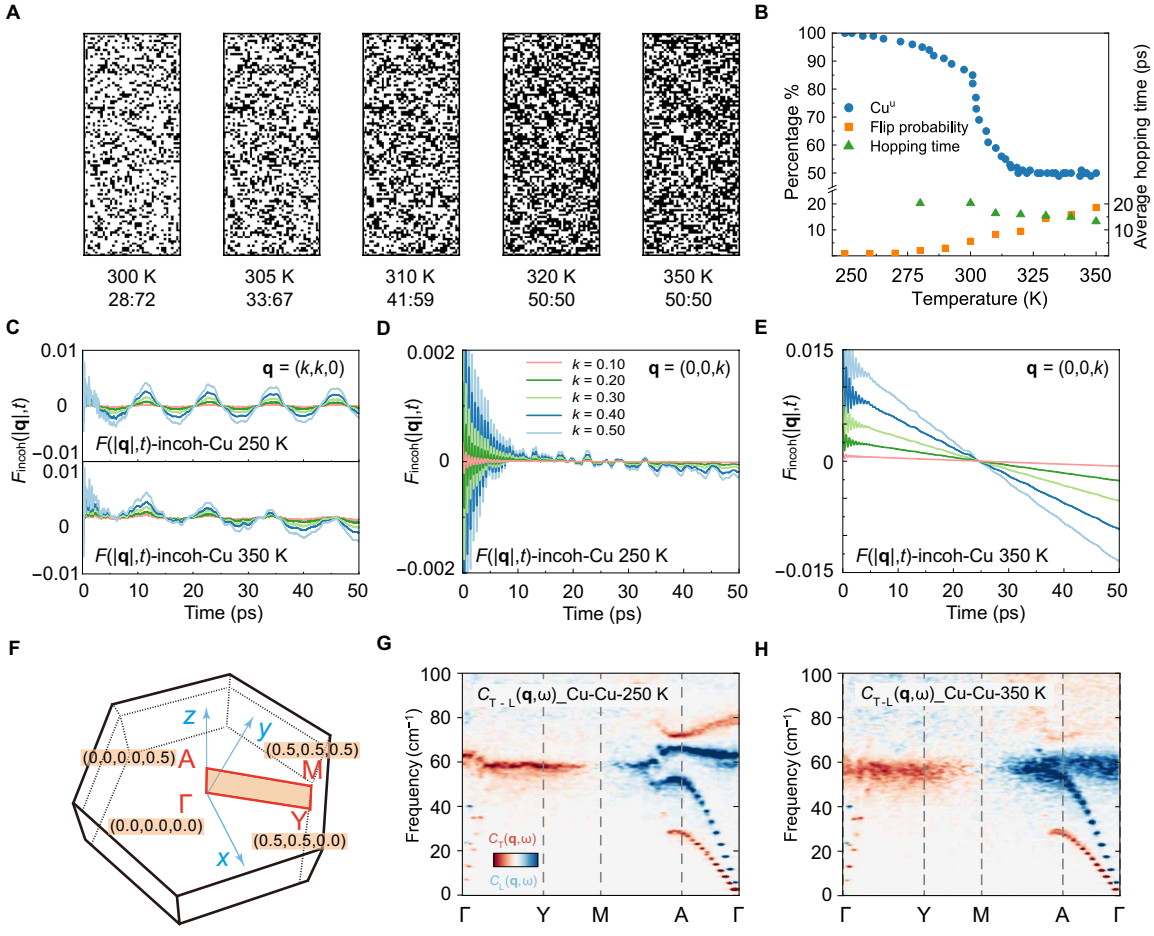

Fig. 4. Disordering and interruptive waves of the Cu sublattice. (**A**) Projection of Cu^+ ion distributions in the CIPS supercell into (110) plane. Black dots and white dots represent the Cu^d and Cu^u, respectively, with their ratio of population provided in the bottom. (**B**) The flip probability and average hopping time of the Cu^+ as a function of temperature. (**C** to **E**) Time evolution of the incoherent intermediate scattering function $F_{incoh}(|\mathbf{q}|,t)$ for the Cu^+ ions at 250 and 350 K along in-plane (k, k, 0) and out-of-plane (0, 0, k) directions with k denoting the wave vector component (in unit of per angstrom) along the respective Cartesian axes. (**F**) Bulk Brillouin zone of CIPS with high-symmetry points marked and the xy plane is the basal plane of CIPS. (**G** and **H**) The difference between the transverse and longitudinal current correlation functions of the Cu-Cu pair [$C_{T\text{-}L}(\mathbf{q},\omega)$] along high-symmetry directions at 250 and 350 K, respectively, with red indicating transverse dominance and blue indicating longitudinal dominance.

compared to the Cu-Cu due to their immobilized and covalent bonding (figs. S25 and S26).

DISCUSSION

It is noteworthy that the suppression of transverse phonon branches in a real liquid necessitates that the characteristic timescale of microscopic relaxation processes (e.g., atomic rearrangements, rotational diffusion, or similar mechanisms) be comparable to or shorter than the transverse vibrational Debye period (*3*) (τ_D). The τ of the Cu hopping in CIPS at 350 K is estimated to be 18.67 ps, much longer than its τ_D of 1.02 ps (see details in Methods), explaining the persistence of long-wavelength transverse acoustic modes. The vertical shuttling of encaged Cu^+ ions between the up and down docking states introduces strong temporal fluctuations in the local bonding environments of the $[P_2S_6]^{4-}$ backbone, which perturb lattice vibrations and enhance multiphonon scattering, thereby amplifying lattice anharmonicity. In CIPS, the discrete dual-docking sites arranged in a 2D configuration suppress configurational entropy compared to the connected, continuous states of disordering-hopping ions in 3D solids, thereby likely reducing segregation by lowering the thermodynamic driving force through enthalpic compensation. Designing solid systems embedded with disconnected passage and finite discrete state for disordering dynamics would be a unique category for pursing high anharmonicity while lowering the threats of decomposition and segregation.

METHODS

Experiment

Bulk CIPS crystals were synthesized using a standard chemical vapor transport method in a two-zone furnace (Hefei Kejing OTF-1200X II). Stoichiometric amounts of elemental Cu, In, P, and S powders were sealed in a quartz tube under vacuum at a base pressure of 10^{-4} Pa. The tube was then positioned in a two-zone furnace with a temperature gradient of 750° to 650°C. The crystals were grown over the course of 1 week and then naturally cooled to room temperature,

forming large, yellow, transparent crystals with a plate-like structure. Raman spectroscopy was conducted using a Horiba LABHRev-UV micro-Raman system with a 633 nm excitation source.

DFT calculations

First-principles calculations were carried out with the projector augmented wave (PAW) method implemented in the Vienna Ab initio Simulation Package (*35*, *36*). The exchange-correlation functional was treated with generalized gradient approximation parametrized by Perdew-Burke-Ernzerhof (*37*) with a plane-wave cutoff energy of 500 eV. The PAW pseudopotentials considered 11 valence electrons for Cu ($3d^{10}$ $4s^1$), 3 for In ($5s^2$ $5p^1$), 5 for P ($3s^2$ $3p^3$), and 6 for S ($3s^2$ $3p^4$). To account for the weak vdW interactions between the CIPS layers, the zero-damping D3 method of Grimme *et al.* (*38*) was used. Geometry optimizations were performed with convergence criteria of 10^{-7} eV for energy and 10^{-5} eV/Å for force. The calculations were conducted on both a monoclinic unit cell and a 2 by 2 by 2 supercell (160 atoms) using Monkhorst-Pack (*39*) k-point grids of 8 by 8 by 8 and 2 by 2 by 2, respectively. The Debye temperature was calculated using the elastic constants method (*40*), with a k-point grid of 15 by 15 by 8. Strain magnitudes ranging from −0.015 to 0.015 were applied to determine the elastic constants and derive the Debye temperature. The transverse vibrational Debye period τ_D is given by $\tau_D = \left(\frac{6\pi^2 N}{V}\right)^{1/3} c_t$, where N is the number of atoms in the unit cell, V is the unit cell volume, and c_t is the effective transverse sound velocity.

Moment tensor potential

The MTP used in this study was developed using the Machine-Learning Interatomic Potentials (MLIP) package (*24*). The training dataset was obtained from ab initio molecular dynamics (AIMD) simulations on 2 by 2 by 2 CIPS supercells for both the paraelectric and ferroelectric phases. Each AIMD simulation used a time step of 2 fs and ran for a total of 5 ps at various temperatures. Low-temperature simulations enhanced sampling near the ground state, while high-temperature simulations captured atomic environments with larger deformations and structural instability, which is critical for investigating Cu ion hopping. AIMD simulations covered temperatures ranging from 50 to 350 K in 100 K increments for both phases. Additional high-temperature data, spanning 400 to 800 K in 100 K increments, was included specifically for the paraelectric phase to capture a broader range of configurations. For ShengBTE force constant construction, the training dataset focused primarily on the ferroelectric phase, whereas MD calculations covered a wide range of paraelectric configurations to accurately characterize the phase transition process. During the training process, the fitting weights for energies ($w_e = 1$), forces ($w_f = 0.01$), and stresses ($w_s = 0.001$) were selected, with a training level of 22 untrained MTP. To mitigate overfitting, every 15th structure was sampled, and 10% of the dataset was reserved for testing. Key structures with high extrapolation grades (*41*) were filtered and included to the secondary training data.

Boltzmann transport equations

The κ_l of CIPS is obtained within the framework of BTE with the formula below

$$\kappa_l = \frac{1}{k_B T^2 \Omega N_{\mathbf{q}}} \sum_{p\mathbf{q}} f^0_{p\mathbf{q}}\left(f^0_{p\mathbf{q}} + 1\right) \times \left(\hbar\omega_{p\mathbf{q}}\right)^2 \mathbf{v}_{p\mathbf{q}} \otimes \mathbf{v}_{p\mathbf{q}} \tau_{p\mathbf{q}} \quad (3)$$

where k_B,T,Ω,$N_{\mathbf{q}}$, and $\hbar$ are the Boltzmann constant, temperature, volume of the unit cell, regular grid of $\mathbf{q}$ points, and the Planck's constant, respectively. $f^0_{p\mathbf{q}}$ is the Bose-Einstein distribution function of phonon mode p with its wave vector of $\mathbf{q}$. $\omega_{p\mathbf{q}}$ is the phonon frequency, $\mathbf{v}_{p\mathbf{q}}$ is the group velocity, and $\tau_{p\mathbf{q}}$ is the phonon lifetime. The third-order and fourth-order force constants are extracted from the trained MTP potential with supercell 5 by 5 by 2 and 2 by 2 by 2 respectively. For the third and fourth constant extrapolation, we used the modified "fake_vasp_calcs.py" (*42*) script to build MTP/ShengBTE interface. The neighboring atoms 12 and 3 are included in interactions, and 2256 and 8144 DFT runs are created, respectively. To produce convergent results, ShengBTE (*43*) and FourPhonon (*44*) were used with a $\mathbf{q}$ grid of 15 by 15 by 15 (third) and 7 by 7 by 7 (fourth) to calculate the κ_l, phonon dynamics, including the weighted phase space, phonon lifetime, and Grüneisen parameters.

MD simulations

Classical MD simulations with MTP were performed using the Large-Scale Atomic/Molecular Massively Parallel Simulator (LAMMPS) package (*44*). Temperature control was maintained using a Nose-Hoover thermostat (*45*). The isothermal–isobaric (NPT) ensemble was used to account for thermal expansion with rising temperatures. A 10 by 10 by 10 supercell was constructed to calculate the temporally and spatially averaged displacement of ions (Fig. 1B) within the NPT ensemble at a temperature range from 100 to 350 K, using a time step of 1 fs and a total simulation time of 10 ns. The averaged displacement component is defined as

$$\overline{\Delta r}_\alpha(T) = \frac{1}{N_i N_t} \sum_{i=1}^{N_i} \sum_{t=1}^{N_t} \left[r_{i\alpha}(t,T) - r^{eq}_{i\alpha}\right], \quad \alpha \in \{x, y, z\} \quad (4)$$

where $r_{i\alpha}(t, T)$ is the instantaneous coordinate of the ith Cu ion at time step t, $r^{eq}_{i\alpha}$ is its relaxed equilibrium coordinate, N_i is the number of Cu ions included, and N_t is the number of MD snapshots.

Independent simulations were performed to generate probability density contours for Cu ions (Fig. 1D) at 150, 250, 300, 305, 320, and 350 K, using a time step of 2 fs under the NPT ensemble, with each simulation running for 5 ns. A larger 10 by 10 by 20 supercell (thickness of 26.5 nm, 40 layers) was constructed and equilibrated for 4 ns at 250 K using the NPT ensemble with a 2 fs timestep. Subsequent simulations within the 250 to 350 K range over 36 ns captured the equilibrium hopping process of Cu ions (Figs. 3B and 4, A and B). For calculating the κ_l using the GK-EMD method, an 8 by 8 by 8 supercell was chosen to mitigate size effects. The centroid atomic stress (*46*) was used to efficiently compute heat flux. Ten independent runs were performed to achieve stable averaged κ_l. The total simulation time was 10 ns, deemed sufficient for convergence. Initially, 1 ns of NPT simulation was performed to relax the structure at a fixed temperature, followed by 9 ns of NVE ensemble simulation to generate an instantaneous heat current.

The PDR of CIPS at 250 K was obtained by projecting atomic velocities onto the phonon eigenvectors from MD trajectories using DynaPhoPy (*47*).

The particle density $n(\mathbf{r},t)$ is defined as

$$n(\mathbf{r}, t) = \sum_{i=1}^{N} \delta[\mathbf{r} - \mathbf{r}_i(t)] \quad (5)$$

where N is the total number of particles, and $\mathbf{r}_i(t)$ represents the position of particle i at time t.

The radial distribution function is defined as

$$g(r)=\frac{n(\mathbf{r})}{\rho\cdot 4\pi r^2\Delta r}\sum_{i=1}^{N}\delta\ [r-|\mathbf{r}_i(t)-r_0|] \tag{6}$$

where ρ is the average particle density of the system, $4\pi r^2\Delta r$ is the volume of the spherical shell at distance r with thickness Δr.

The average hopping time, T_{hopping}, is defined as the average interval between consecutive hopping events for particles as follows

$$T_{\text{hopping}}=\frac{\sum_{i=1}^{N}\Delta t_i}{N} \tag{7}$$

where N is the total number of hopping events, Δt_i represents the time interval between two consecutive hopping events for a single particle.

The intermediate scattering function $F(\mathbf{q},t)$ is derived as the Fourier transform of the autocorrelation function of the particle density

$$F(\mathbf{q},t)=\frac{1}{N}\langle n(\mathbf{q},t)n(-\mathbf{q},0)\rangle=\frac{1}{N}\sum_{i}^{N}\sum_{j}^{N}\left\langle\exp\{i\mathbf{q}\cdot[\mathbf{r}_i(t)-\mathbf{r}_j(0)]\}\right\rangle \tag{8}$$

where $\mathbf{q}$ denotes the wave vector. The angular brackets $\langle\cdot\rangle$ indicate an ensemble average. The function $F(\mathbf{q},t)$ is typically referred to as the coherent intermediate scattering function.

The current density, defined as a vector split into transverse and longitudinal components, was calculated as follows

$$\mathbf{j}(\mathbf{r},t)=\sum_{i}^{N}\mathbf{s}_i(t)\delta\ [\mathbf{r}-\mathbf{r}_i(t)] \tag{9}$$

$$\mathbf{j}(\mathbf{q},t)=\sum_{i}^{N}\mathbf{s}_i(t)e^{i\mathbf{q}\cdot\mathbf{r}_i(t)}=\mathbf{j}_{\text{longitudinal}}(\mathbf{q},t)+\mathbf{j}_{\text{transverse}}(\mathbf{q},t) \tag{10}$$

where $\mathbf{r}_i(t)$ is the position of atom i at time t and N is the total number of atoms. $\mathbf{s}_i(t)$ is the velocity of atom i at time t. The current correlation functions can be computed as (*48*)

$$C_{\text{L}}(\mathbf{q},t)=\frac{1}{N}\left\langle\mathbf{j}_{\text{L}}(\mathbf{q},t)\cdot\mathbf{j}_{\text{L}}(-\mathbf{q},0)\right\rangle \tag{11}$$

$$C_{\text{T}}(\mathbf{q},t)=\frac{1}{N}\left\langle\mathbf{j}_{\text{T}}(\mathbf{q},t)\cdot\mathbf{j}_{\text{T}}(-\mathbf{q},0)\right\rangle \tag{12}$$

For this investigation, we used a 14 by 14 by 14 supercell containing 54,880 atoms to compute the longitudinal and transverse current correlation functions using MD trajectories at 250 and 350 K.

Supplementary Materials

This PDF file includes:

Figs. S1 to S29
Tables S1 and S2
References

REFERENCES

1. Q. Ren, M. K. Gupta, M. Jin, J. Ding, J. Wu, Z. Chen, S. Lin, O. Fabelo, J. A. Rodríguez-Velamazán, M. Kofu, K. Nakajima, M. Wolf, F. Zhu, J. Wang, Z. Cheng, G. Wang, X. Tong, Y. Pei, O. Delaire, J. Ma, Extreme phonon anharmonicity underpins superionic diffusion and ultralow thermal conductivity in argyrodite Ag_8SnSe_6. *Nat. Mater.* **22**, 999–1006 (2023).
2. H. Hu, Y. Ju, J. Yu, Z. Wang, J. Pei, H. C. Thong, J. W. Li, B. Cai, F. Liu, Z. Han, B. Su, H. L. Zhuang, Y. Jiang, H. Li, Q. Li, H. Zhao, B. P. Zhang, J. Zhu, J. F. Li, Highly stabilized and efficient thermoelectric copper selenide. *Nat. Mater.* **23**, 527–534 (2024).
3. K. Trachenko, Heat capacity of liquids: An approach from the solid phase. *Phys. Rev. B* **78**, 104201 (2008).
4. B. Li, H. Wang, Y. Kawakita, Q. Zhang, M. Feygenson, H. L. Yu, D. Wu, K. Ohara, T. Kikuchi, K. Shibata, T. Yamada, X. K. Ning, Y. Chen, J. Q. He, D. Vaknin, R. Q. Wu, K. Nakajima, M. G. Kanatzidis, Liquid-like thermal conduction in intercalated layered crystalline solids. *Nat. Mater.* **17**, 226–230 (2018).
5. H. Liu, X. Shi, F. Xu, L. Zhang, W. Zhang, L. Chen, Q. Li, C. Uher, T. Day, G. J. Snyder, Copper ion liquid-like thermoelectrics. *Nat. Mater.* **11**, 422–425 (2012).
6. J. Ma, O. Delaire, A. F. May, C. E. Carlton, M. A. McGuire, L. H. VanBebber, D. L. Abernathy, G. Ehlers, T. Hong, A. Huq, W. Tian, V. M. Keppens, Y. Shao-Horn, B. C. Sales, Glass-like phonon scattering from a spontaneous nanostructure in $AgSbTe_2$. *Nat. Nanotechnol.* **8**, 445–451 (2013).
7. K. Miyata, T. L. Atallah, X.-Y. Zhu, Lead halide perovskites: Crystal-liquid duality, phonon glass electron crystals, and large polaron formation. *Sci. Adv.* **3**, e1701469 (2017).
8. J. L. Niedziela, D. Bansal, A. F. May, J. Ding, T. Lanigan-Atkins, G. Ehlers, D. L. Abernathy, A. Said, O. Delaire, Selective breakdown of phonon quasiparticles across superionic transition in $CuCrSe_2$. *Nat. Phys.* **15**, 73–78 (2019).
9. J. Ding, M. K. Gupta, C. Rosenbach, H. M. Lin, N. C. Osti, D. L. Abernathy, W. G. Zeier, O. Delaire, Liquid-like dynamics in a solid-state lithium electrolyte. *Nat. Phys.* **21**, 118–125 (2025).
10. P. Qiu, M. T. Agne, Y. Liu, Y. Zhu, H. Chen, T. Mao, J. Yang, W. Zhang, S. M. Haile, W. G. Zeier, J. Janek, C. Uher, X. Shi, L. Chen, G. J. Snyder, Suppression of atom motion and metal deposition in mixed ionic electronic conductors. *Nat. Commun.* **9**, 2910 (2018).
11. H. Zhu, K. Miyata, Y. Fu, J. Wang, P. P. Joshi, D. Niesner, K. W. Williams, S. Jin, X. Y. Zhu, Screening in crystalline liquids protects energetic carriers in hybrid perovskites. *Science* **353**, 1409–1413 (2016).
12. A. Bhui, K. Biswas, Mobile ion confinement for better thermoelectrics. *Nat. Mater.* **23**, 451–452 (2024).
13. D. J. Voneshen, H. C. Walker, K. Refson, J. P. Goff, Hopping time scales and the phonon-liquid electron-crystal picture in thermoelectric copper selenide. *Phys. Rev. Lett.* **118**, 145901 (2017).
14. D. Yang, X. Su, J. Li, H. Bai, S. Wang, Z. Li, H. Tang, K. Tang, T. Luo, Y. Yan, J. Wu, J. Yang, Q. Zhang, C. Uher, M. G. Kanatzidis, X. Tang, Blocking ion migration stabilizes the high thermoelectric performance in Cu_2Se composites. *Adv. Mater.* **32**, e2003730 (2020).
15. A. J. E. Rettie, J. Ding, X. Zhou, M. J. Johnson, C. D. Malliakas, N. C. Osti, D. Y. Chung, R. Osborn, O. Delaire, S. Rosenkranz, M. G. Kanatzidis, A two-dimensional type I superionic conductor. *Nat. Mater.* **20**, 1683–1688 (2021).
16. X. Jiang, X. Zhang, Z. Deng, J. Deng, X. Wang, X. Wang, W. Yang, Dual-role ion dynamics in ferroionic $CuInP_2S_6$: Revealing the transition from ferroelectric to ionic switching mechanisms. *Nat. Commun.* **15**, 10822 (2024).
17. X.-Q. Yan, X. Zhao, H. Xu, L. Zhang, D. Liu, Y. Zhang, C. Huo, F. Liu, J. Xie, X. Dong, Z. B. Liu, J. G. Tian, Temperature-tunable optical properties and carrier relaxation of $CuInP_2S_6$ crystals under ferroelectric-paraelectric phase transition. *J. Mater. Chem. C* **10**, 696–706 (2022).
18. S. Lee, P. Colombet, G. Ouvrard, R. Brec, General trends observed in the substituted thiophosphate family. Synthesis and structure of silver scandium thiophosphate, $AgScP_2S_6$, and cadmium iron thiophosphate, $CdFeP_2S_6$. *Inorg. Chem.* **27**, 1291–1294 (1988).
19. J. K. Burdett, O. Eisenstein, From three- to four-coordination in copper(I) and silver(I). *Inorg. Chem.* **31**, 1758–1762 (1992).
20. S.-H. Wei, S. B. Zhang, A. Zunger, Off-center atomic displacements in zinc-blende semiconductor. *Phys. Rev. Lett.* **70**, 1639–1642 (1993).
21. K. Chang, J. Liu, H. Lin, N. Wang, K. Zhao, A. Zhang, F. Jin, Y. Zhong, X. Hu, W. Duan, Q. Zhang, L. Fu, Q. K. Xue, X. Chen, S. H. Ji, Discovery of robust in-plane ferroelectricity in atomic-thick SnTe. *Science* **353**, 274–278 (2016).
22. S. Zhou, L. You, H. Zhou, Y. Pu, Z. Gui, J. Wang, Van der Waals layered ferroelectric $CuInP_2S_6$: Physical properties and device applications. *Front. Phys.* **16**, 13301 (2020).
23. K. J. Choi, M. Biegalski, Y. L. Li, A. Sharan, J. Schubert, R. Uecker, P. Reiche, Y. B. Chen, X. Q. Pan, V. Gopalan, L. Q. Chen, D. G. Schlom, C. B. Eom, Enhancement of ferroelectricity in strained $BaTiO_3$ thin films. *Science* **306**, 1005–1009 (2004).
24. I. S. Novikov, K. Gubaev, E. V. Podryabinkin, A. V. Shapeev, The MLIP package: Moment tensor potentials with MPI and active learning. *Mach. Learn. Sci. Technol.* **2**, 025002 (2021).

25. V. Maisonneuve, V. B. Cajipe, A. Simon, R. Von Der Muhll, J. Ravez, Ferrielectric ordering in lamellar $CuInP_2S_6$. *Phys. Rev. B* **56**, 10860–10868 (1997).
26. A. Kohutych, V. Liubachko, V. Hryts, Y. Shiposh, M. Kundria, M. Medulych, K. Glukhov, R. Yevych, Y. Vysochanskii, Phonon spectra and phase transitions in van der Waals ferroics $MM'P_2X_6$. *Mol. Cryst. Liq. Cryst.* **747**, 14–22 (2022).
27. V. Liubachko, V. Shvalya, A. Oleaga, A. Salazar, A. Kohutych, A. Pogodin, Y. M. Vysochanskii, Anisotropic thermal properties and ferroelectric phase transitions in layered $CuInP_2S_6$ and $CuInP_2Se_6$ crystals. *J. Phys. Chem. Solids* **111**, 324–327 (2017).
28. V. Liubachko, A. Oleaga, A. Salazar, A. Kohutych, K. Glukhov, A. Pogodin, Y. Vysochanskii, Cation role in the thermal properties of layered materials $M^{1+}M^{3+}P_2(S, Se)_6$ (M^{1+} = Cu, Ag; M^{3+} = In, Bi). *Phys. Rev. Mater.* **3**, 104415 (2019).
29. T. Feng, X. Ruan, Four-phonon scattering reduces intrinsic thermal conductivity of graphene and the contributions from flexural phonons. *Phys. Rev. B* **97**, 045202 (2018).
30. S. Bi, Z. Chang, K. Yuan, Z. Sun, X. Zhang, Y. Gao, D. Tang, First-principles prediction of the lattice thermal conductivity of two-dimensional (2D) h-BX (X = P, As, Sb) considering the effects of fourth-order and all-order scattering. *J. Appl. Phys.* **132**, 114301 (2022).
31. Z. Han, X. Ruan, Thermal conductivity of monolayer graphene: Convergent and lower than diamond. *Phys. Rev. B* **108**, L121412 (2023).
32. J. A. Brehm, S. M. Neumayer, L. Tao, A. O'Hara, M. Chyasnavichus, M. A. Susner, M. A. McGuire, S. V. Kalinin, S. Jesse, P. Ganesh, S. T. Pantelides, P. Maksymovych, N. Balke, Tunable quadruple-well ferroelectric van der Waals crystals. *Nat. Mater.* **19**, 43–48 (2020).
33. Z. Fan, L. F. C. Pereira, H. Q. Wang, J. C. Zheng, D. Donadio, A. Harju, Force and heat current formulas for many-body potentials in molecular dynamics simulations with applications to thermal conductivity calculations. *Phys. Rev. B* **92**, 094301 (2015).
34. V. Samulionis, Y. Vysochanskii, V. Cajipe, Ultrasonic and piezoelectric investigation of $Sn_2P_2S_6$ type photosensitive ferroelectric-semiconductor crystals. *Ferroelectrics* **295**, 21–30 (2003).
35. G. Kresse, J. Furthmüller, Efficient iterative schemes for ab initio total-energy calculations using a plane-wave basis set. *Phys. Rev. B* **54**, 11169–11186 (1996).
36. G. Kresse, D. Joubert, From ultrasoft pseudopotentials to the projector augmented-wave method. *Phys. Rev. B* **59**, 1758–1775 (1999).
37. J. P. Perdew, K. Burke, M. Ernzerhof, Generalized gradient approximation made simple. *Phys. Rev. Lett.* **77**, 3865–3868 (1996).
38. S. Grimme, J. Antony, S. Ehrlich, H. Krieg, A consistent and accurate ab initio parametrization of density functional dispersion correction (DFT-D) for the 94 elements H-Pu. *Chem. Phys.* **132**, 154104 (2010).
39. H. J. Monkhorst, J. D. Pack, Special points for Brillouin-zone integrations. *Phys. Rev. B* **13**, 5188–5192 (1976).
40. O. L. Anderson, A simplified method for calculating the debye temperature from elastic constants. *J. Phys. Chem. Solids* **24**, 909–917 (1963).
41. E. V. Podryabinkin, A. V. Shapeev, Active learning of linearly parametrized interatomic potentials. *Comput. Mater. Sci.* **140**, 171–180 (2017).
42. B. Mortazavi, E. V. Podryabinkin, S. Roche, T. Rabczuk, X. Zhuang, A. V. Shapeev, Machine-learning interatomic potentials enable first-principles multiscale modeling of lattice thermal conductivity in graphene/borophene heterostructures. *Mater. Horiz.* **7**, 2359–2367 (2020).
43. W. Li, J. Carrete, N. A. Katcho, N. Mingo, ShengBTE: A solver of the Boltzmann transport equation for phonons. *Comput. Phys. Commun.* **185**, 1747–1758 (2014).
44. A. P. Thompson, H. M. Aktulga, R. Berger, D. S. Bolintineanu, W. M. Brown, P. S. Crozier, P. J. in 't Veld, A. Kohlmeyer, S. G. Moore, T. D. Nguyen, R. Shan, M. J. Stevens, J. Tranchida, C. Trott, S. J. Plimpton, LAMMPS—A flexible simulation tool for particle-based materials modeling at the atomic, meso, and continuum scales. *Comput. Phys. Commun.* **271**, 108171 (2022).
45. S. Nosé, A unified formulation of the constant temperature molecular dynamics methods. *J. Chem. Phys.* **81**, 511–519 (1984).
46. D. Surblys, H. Matsubara, G. Kikugawa, T. Ohara, Application of atomic stress to compute heat flux via molecular dynamics for systems with many-body interactions. *Phys. Rev. E* **99**, 051301 (2019).
47. A. Carreras, A. Togo, I. Tanaka, DynaPhoPy: A code for extracting phonon quasiparticles from molecular dynamics simulations. *Comput. Phys. Commun.* **221**, 221–234 (2017).
48. E. Fransson, M. Slabanja, P. Erhart, G. Wahnström, dynasor—A tool for extracting dynamical structure factors and current correlation functions from molecular dynamics simulations. *Adv. Theory Simul.* **4**, 2000240 (2021).
49. B. Mortazavi, I. S. Novikov, E. V. Podryabinkin, S. Roche, T. Rabczuk, A. V. Shapeev, X. Zhuang, Exploring phononic properties of two-dimensional materials using machine learning interatomic potentials. *Appl. Mater. Today* **20**, 100685 (2020).
50. A. Togo, I. Tanaka, First principles phonon calculations in materials science. *Scr. Mater.* **108**, 1–5 (2015).
51. H. Zhan, Y. Nie, Y. Chen, J. M. Bell, Y. Gu, Thermal transport in 3D nanostructures. *Adv. Funct. Mater.* **30**, 1903841 (2020).

Acknowledgments: This work was performed at the High Performance Computing Cluster (HPCC), which is supported by the Information and Communication Technology Office (ICTO) of the University of Macau. We appreciate Y. Vysochanskii from Uzhhorod National University for sharing the κ_l experiment data. We appreciate Y. Zhou from Hong Kong University of Science and Technology for the discussion of Green-Kubo formula and S. Singh from Rutgers University for offering of POSCAR file. **Funding:** This work was supported by the National Natural Science Foundation of China (grant 22022309); Natural Science Foundation of Guangdong Province, China (2024A1515011161); University of Macau (MYRG-GRG2024-00028-IAPME and MYRG-GRG2025-00045-IAPME); and Science and Technology Development Fund from Macau SAR (0122/2024/AFJ and 0120/2023/RIA2). **Author contributions:** B.W.: Methodology, software, formal analysis, investigation, visualization, data curation, writing—original draft, and writing—review and editing; H.Y.: Software, data curation, methodology, formal analysis, and visualization; J.H.: Formal analysis, investigation, software, and validation; X.Y.: Methodology and formal analysis; C.H.: Investigation and formal analysis; J.L.: Formal analysis and writing—review and editing; Q.K. and Y.C.: Conceptualization, funding acquisition, resources, supervision, writing—original draft, and writing—review and editing. **Competing interests:** The authors declare that they have no competing interests. **Data, code, and materials availability:** All data and code needed to evaluate and reproduce the results in the paper are present in the paper and/or the Supplementary Materials. This study did not generate new materials.

Submitted 21 November 2025
Accepted 4 March 2026
Published 1 April 2026
10.1126/sciadv.aee1289

ScienceAdvances

Dynamic disordering in discrete states: Disconnected hopping boosts anharmonicity in $CuInP_2S_6$

Bowen Wang, Hejin Yan, Jie Huang, Xuefei Yan, Changmeng Huan, Johannes Lischner, Qingqing Ke, and Yongqing Cai

Sci. Adv. **12** (14), eaee1289. DOI: 10.1126/sciadv.aee1289